# Constraints on seismic velocities in the Earth from traveltimes

# B. L. N. Kennett,[1] E. R. Engdahl[2] and R. Buland[2]

[1]*Research School of Earth Sciences, Australian National University, Canberra* ACT 0200, *Australia*
[2]*National Earthquake Information Center, US Geological Survey, Denver Federal Center*, Box 25046, MS 967, *Denver*, CO 80225, *USA*

## SUMMARY

New empirical traveltime curves for the major seismic phases have been derived from the catalogues of the International Seismological Centre by relocating events by using *P* readings, depth phases and the *iasp91* traveltimes, and then re-associating phase picks. A smoothed set of traveltime tables is extracted by a robust procedure which gives estimates of the variance of the traveltimes for each phase branch. This set of smoothed empirical times is then used to construct a range of radial velocity profiles, which are assessed against a number of different measures of the level of fit between the empirical times and the predictions of the models. These measures are constructed from weighted sums of $L_2$ misfits for individual phases. The weights are chosen to provide a measure of the probable reliability of the picks for the different phases.

A preferred model, *ak135*, is proposed which gives a significantly better fit to a broad range of phases than is provided by the *iasp91* and *sp6* models. The differences in velocity between *ak135* and these models are generally quite small except at the boundary of the inner core, where reduced velocity gradients are needed to achieve satisfactory performance for *PKP* differential time data.

The potential resolution of velocity structure has been assessed with the aid of a non-linear search procedure in which 5000 models have been generated in bounds about *ak135*. Misfit calculations are performed for each of the phases in the empirical traveltime sets, and the models are then sorted using different overall measures of misfit. The best 100 models for each criterion are displayed in a model density plot which indicates the consistency of the different models. The interaction of information from different phases can be analysed by comparing the different misfit measures. Structure in the mantle is well resolved except at the base, and *ak135* provides a good representation of core velocities.

**Key words:** core phases, *P* waves, *S* waves, seismic velocities, traveltimes.

## 1 INTRODUCTION

The radial structure of the Earth has been a focus of seismological interest for many years, and a wide variety of different techniques have been employed to exploit waves travelling through the mantle and those seismic phases that penetrate the core.

At the core–mantle boundary, there is a large increase in density between the mantle and the core, but a sharp drop in *P*-wave velocity in the core. As a consequence, *P*-wave energy entering the core is refracted sharply towards the vertical. The combined effects of spherical concentration and the increase in seismic velocity with depth eventually turn *P* rays back towards the surface, but a zone of nearly

1000 km extent at the top of the outer core is not sampled by a turning ray. The lower *P* velocities in the core give rise to a strong caustic in *PKP* near 144° epicentral distance, and the presence of the inner core adds further complexity to the propagation pattern of *PKP* and the core multiples such as *PKKP*.

By contrast, the *P*-wave velocity in the core is slightly higher than the *S*-wave velocity in the mantle, so that a faster path exists in the core, and *SKS*, *SKKS* and higher order core multiples sample the whole of the core.

Thus, if we are to constrain the compressional-wave velocities in the core using body-wave arrivals, we have to have high confidence in both the *P* and *S* velocity distributions in the mantle. The problems are compounded

by the traveltime cross-over between *S* and *SKS* near 80°, which makes it difficult to obtain direct information on the *S* velocity distribution in the lower part of the mantle.

An alternative approach is to construct radial velocity profiles for the whole Earth by matching the observed eigenfrequencies of normal modes. However, since the frequencies of the available modes lie below 0.0125 Hz, the available resolution in depth is limited. Dziewonski, Hales & Lapwood (1975) with the *pem* model attempted to improve resolution by incorporating traveltime information, and this procedure was extended by Dziewonski & Anderson (1981) with the *prem* model. More recently, Widmer (1991) has exploited the improved accuracy of modal eigenfrequency determination to derive the model *core11* purely from the normal-mode data; *core11* has only minor deviations from *prem* in the core.

The extensive catalogue of events and arrival times collected by the International Seismological Centre (ISC) has recently been exploited to generate models based on traveltime information. Kennett & Engdahl (1991) developed the *iasp91* model, for which the mantle velocity distributions were designed to match the observed times of *P* and *S*, whilst the core structure was taken from *pem* with modified radii for the inner and outer cores. Subsequently, Morelli & Dziewonski (1993) attempted to obtain a closer representation of the global average structure with the model *sp6*. The inversion procedure of Morelli & Dziewonski includes *PKP* and *SKS* observations in order to provide an improved core structure.

The advent of high-quality digital data has led to the study of differential times between the branches of *PKP* measured from the same digital seismograms (Creager 1992; Song & Helmberger 1994; McSweeney, Creager & Merrill 1995). Neither *iasp91* nor *sp6* is entirely compatible with the differential time constraints. The work of Song & Helmberger (1994) and Kaneshima *et al.* (1994) suggests that the most likely cause is the form of the structure in the immediate neighbourhood of the inner core boundary.

The present paper makes use of new empirical traveltime curves for all the major seismic phases, which have been derived from the ISC catalogues by relocating events by using *P* readings, depth phases, and the *iasp91* traveltimes. This set of smoothed empirical times is then used to construct a range of radial velocity profiles based on different measures of the level of fit between the empirical times and the predictions of the models. These misfit measures have been constructed by using a weighted sum of $L_2$ misfits for individual phases. The weights are chosen to provide a measure of the likely reliability of the picks for the different phases. By combining information from different phase branch selections, attention can be focused on selected aspects of the velocity structure.

A sequence of velocity models was constructed to remove the *S* baseline problems of *iasp91*, and, to a lesser extent of *sp6*, and then to provide improved fits to the core phases. A preferred model, *ak135*, is proposed which gives a good fit to a broad range of phases and a satisfactory performance for the *PKP* differential time data.

In order to assess the potential resolution of velocity structure, we have carried out a non-linear search procedure in which 5000 models have been generated in bounds about *ak135*. Misfit calculations are performed for each of the

phases in the empirical traveltime sets. The models are then sorted using different overall measures of misfit, and the best 100 models for each criterion are displayed in a model density plot. These results display the interaction of information from different phases and indicate that *ak135* provides a good representation of core velocities.

## 2 EMPIRICAL TRAVELTIMES

The ISC catalogue provides an unparalleled collection of seismic event information and arrival times for a very wide range of phases. The locations provided by the ISC are determined using the Jeffreys & Bullen (1940) traveltime tables. It has been recognized for many years that there was a baseline problem with the Jeffreys & Bullen (JB) tables, because events with independently determined locations show origin-time errors of the order of 2 s. A major effort to improve *P*-wave traveltime tables was made in 1968 (Herrin 1968), but the absence of *S* times limited the usefulness of this set of tables. An initiative by the International Association of Seismology and Physics of the Earth's Interior (IASPEI) to improve earthquake locations led to the construction of the *iasp91* model (Kennett & Engdahl 1991) and the *sp6* model (Morelli & Dziewonski 1993). From these models, traveltimes can be calculated for the full range of seismic phases; the main phases have been tabulated (Kennett 1991) and the same material is available in computational form.

The *P*-wave times for *iasp91* and *sp6* are in very close agreement out to 80°, and both models indicate an average offset of 1.7 s from the JB tables, which is likely to be manifest in the ISC event parameters. In order to improve the estimates of the traveltimes for later phases, the entire set of events in the ISC catalogues from 1964 to 1991 has been relocated using the arrival times for mantle *P* waves and associated depth phases, with the *iasp91* traveltimes. After the relocation, 6000 events with a good geographical and depth distribution over the globe were selected (see Fig. 1). For each event, the reported arrival times are re-associated with the new event parameters (in both space and time) and corrected to surface focus to give a total of approximately 1 679 000 raw traveltimes for the major seismic phases. Although only a relatively small subset of events have been used, this set of arrivals includes about 14 per cent of all the readings in the ISC catalogue.

For each of the seismic phases, the raw traveltimes as a function of epicentral distance are smoothed using a robust procedure which also yields estimates of the variance in the times reported to ISC. Where possible, a smooth interpolation is made over data gaps arising from the limitations of the association process in the presence of crossing arrivals. This procedure works well where there is a large separation in the slowness between the two crossing phases, as for example *ScP* and *S* near 39°. The measures of the standard deviation reflect only the scatter about the smooth times and do not include any assessment of the influence of other factors such as the coda of a preceding arrival on the quality of a time pick.

Table 1 shows the epicentral distance ranges for which the empirical traveltimes have been determined. For a number of phases, the available distance intervals are smaller than might be expected from theoretical considerations, but have
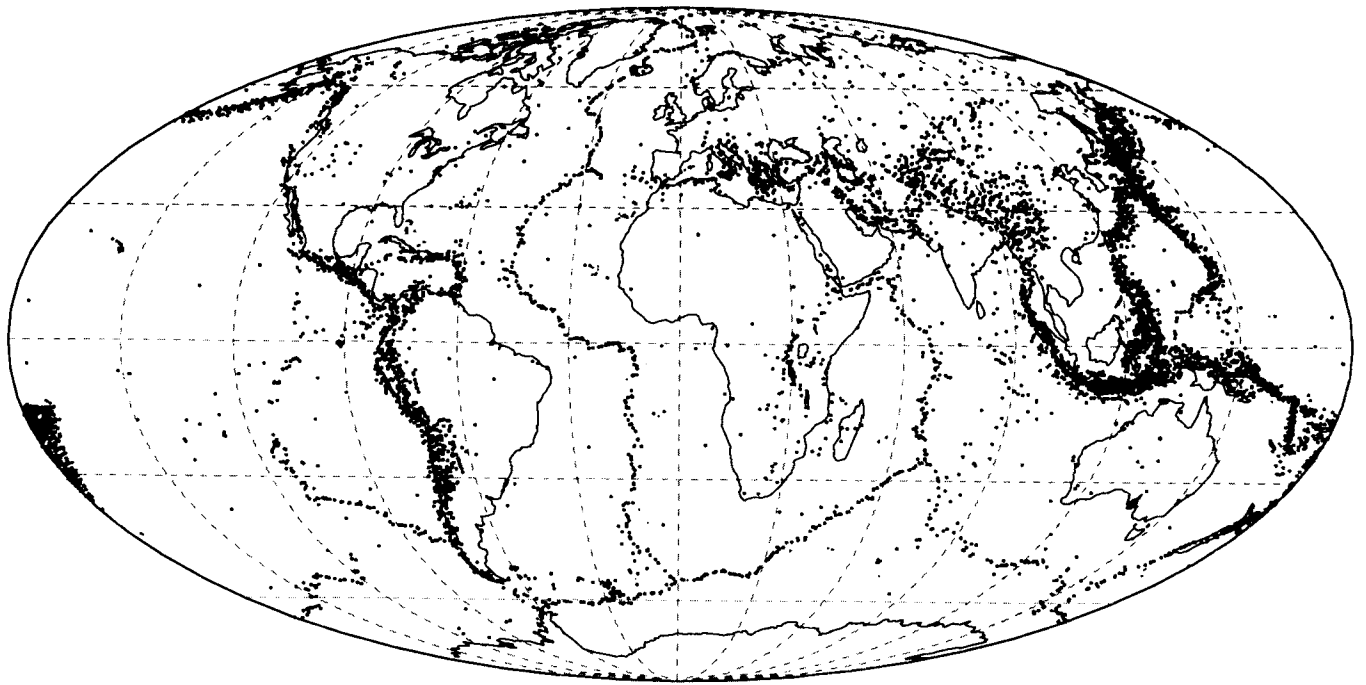
**Figure 1.** Geographical distribution of selected events used in constructing the smoothed empirical traveltimes.

been chosen to ensure a satisfactory separation between different types of arrivals in the process of phase association. Where the slownesses of two crossing phases are rather similar, for example *S*, *SKS* from 80° on, there is a rather

**Table 1.** Observed seismic phases.

| Phase branch | Distance range | Weight |
|---|---|---|
| *P* | 25-99° | 5.0 |
| *Pdiff* | 100-125 ° | 0.0 |
| *S* | 25-80° | 3.0 |
| *Sdiff* | 100-125 ° | 0.0 |
| *PP* | 53-180° | 1.5 |
| *SS* | 56-150° | 1.0 |
| *PcP* | 26-70° | 2.0 |
| *ScS* | 19-65° | 1.0 |
| *ScP* | 18-62° | 2.0 |
| *SP* | 95-128° | 1.0 |
| *PKPdf* | 118-180° | 4.0 |
| *PKPbc* | 151-153° | 4.0 |
| *PKPab* | 156-178° | 4.0 |
| *PKKPab* | 111-122° | 1.5 |
| *PKKPbc* | 83-122° | 1.5 |
| *SKSac* | 91-123° | 3.0 |
| *SKKSac* | 65-178° | 1.5 |
| *SKPdf* | 113-160° | 1.0 |
| *SKPbc* | 141-148° | 1.0 |
| *P'P'* | 56-67, 79-103 ° | 1.0 |

long distance interval in which a reliable phase separation cannot be achieved.

In our subsequent comparisons of the empirical traveltimes with the predictions of radial velocity models, we have excluded two groups of arrivals for which the influence of lateral heterogeneity is likely to make the definition of an 'average' somewhat problematical. We do not include the crustal and upper-mantle *P* and *S* arrivals out to 25°, for which considerable regional variation is well established. Most stations are in continental areas, so that, as in *iasp91*, we adopt a continental style of structure for the crust and uppermost mantle. We also exclude the diffracted waves around the core ($P_{\text{diff}}$, $S_{\text{diff}}$) which are not adequately modelled with a simple ray representation, and which also pass through significant lateral heterogeneity. The progressive loss in high frequencies for these diffracted waves as the epicentral distance increases has the effect of changing the waveform with a consequent change in picking characteristics.

### 2.1 Comparison of empirical times and the *iasp91* model

The *iasp91* model (Kennett & Engdahl 1991) was developed to provide a representation of the times of arrival of the major seismic phases, particularly for use in earthquake location. As we have noted above, the *P* times and depth phases for this model have been used in the relocation procedure which generated the empirical traveltimes from the ISC data set.

Now that we have the smoothed empirical times available for a large number of seismic phases, we can assess the performance of the *iasp91* model. Fig. 2 shows a composite display of the traveltime residuals between the predictions of the *iasp91* model and the empirical times for 18 seismic phases. For each phase, the residuals are plotted at 1°
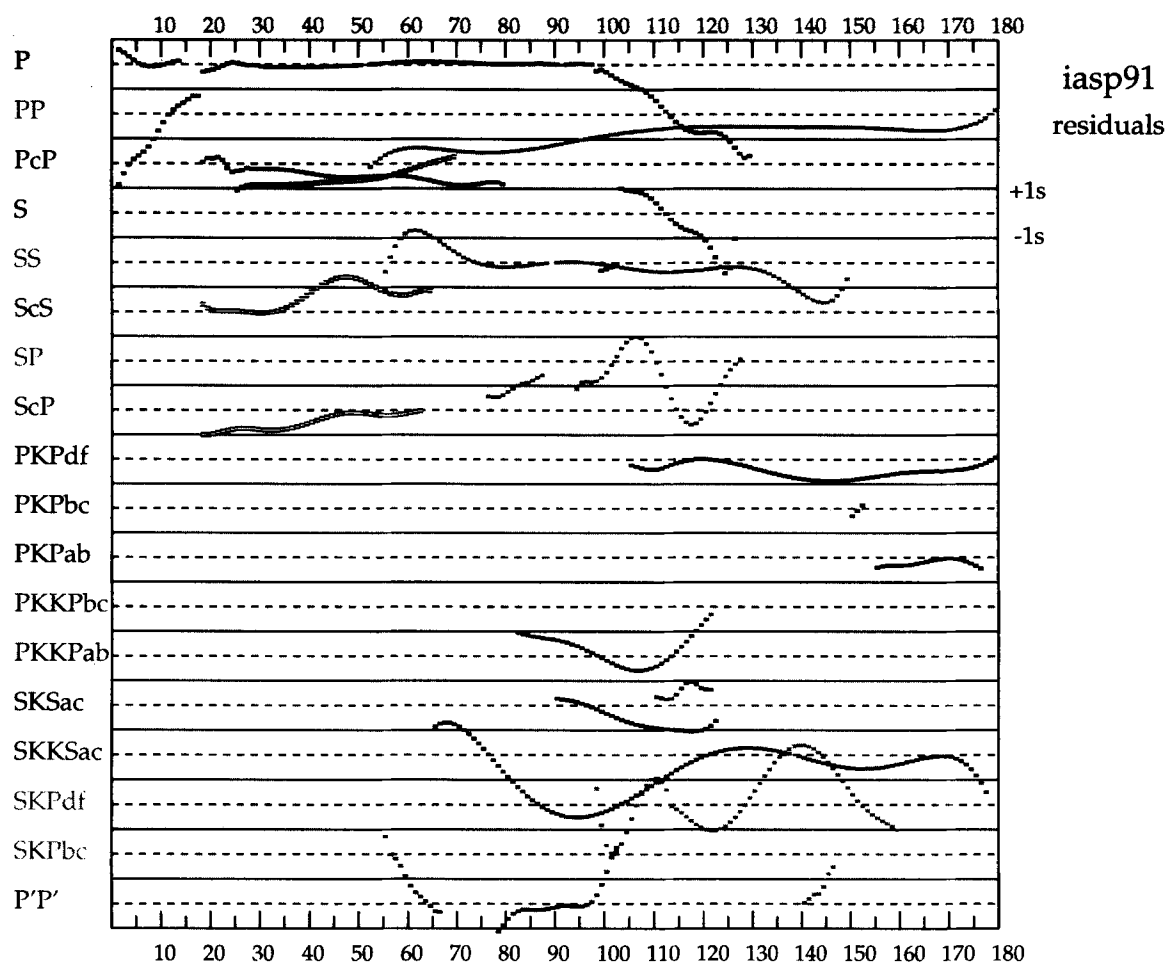
**Figure 2.** Composite display of the residuals between the predictions for model *iasp91* and the smoothed empirical traveltimes. 18 phase branches are displayed simultaneously in a panel of width ±1 s around the empirical time.

intervals with a 2 s outline box extending ±1 s from the empirical times. If the theoretical times are faster, the residuals will be negative. Since some of the residuals exceed 1 s we have used black and two tones of grey to improve the visual separation of the traces.

A composite residual plot such as Fig. 2 contains a great deal of information about the characteristics of the model, but the residuals alone do not provide the whole picture. We need to know the likely error in the smoothed times and the reliability of the construction procedure. In Fig. 3, we therefore display the standard deviation for each of the phases (Fig. 3a) in a similar style of composite display to Fig. 2, and also the logarithmic 'hit-count' associated with each degree interval for each of the phases (Fig. 3b). For *P*, the hit count exceeds 10 000 traveltimes in a 1° bin for much of the interval from 25° to 90°, whereas relatively low numbers of readings were available for *SKP*, *PKPPKP(P'P')*.

The general fit of the *iasp91* times to the empirical times is quite good, with most of the more prominent phases fitted to within the estimates of the standard deviation. Although we have earlier discounted the crustal and upper mantle arrivals for *P* for use in quantitative misfit measures, we note that *iasp91* gives an effective representation out to 25°.

From 25° to 99° the residuals for *P* are small, which indicates the self-consistency of the relocation procedure, but the residuals rapidly increase for the diffracted arrivals.

For *S*, the entire *iasp91* traveltime curve is displaced from the empirical times, indicating a baseline shift of about 1.2 s, arising from an inadequate tie between the *P* and *S* times for *iasp91*. Kennett & Engdahl (1991) noted that, while the shorter-distance times used to constrain the upper mantle were close to an average of different classes of structure for *P*, there was a bias towards tectonic structure for *S*. This bias translates into a baseline offset for the teleseismic arrivals. The general trend of the *S* residuals from 25° to 80° is slightly tilted towards faster times for deeper levels of penetration.

There is also a noticeable discrepancy for *PKIKP* ($PKP_{df}$) for which the predicted time is nearly 1 s early around 145°. The $PKP_{ab}$ and the $PKP_{bc}$ branches are better represented, although the slope of the calculated $PKP_{bc}$ arrivals is discordant with the smoothed empirical times. The other major core phase *SKS* is nearly 1 s early for *iasp91* near 110° despite the delayed baseline for *S*. The misfits for the reflected phases *PcP* and *ScP* are also larger than is desirable. For phases such as *SKP* and *SP* the available data coverage is not large and this results in undulations in the
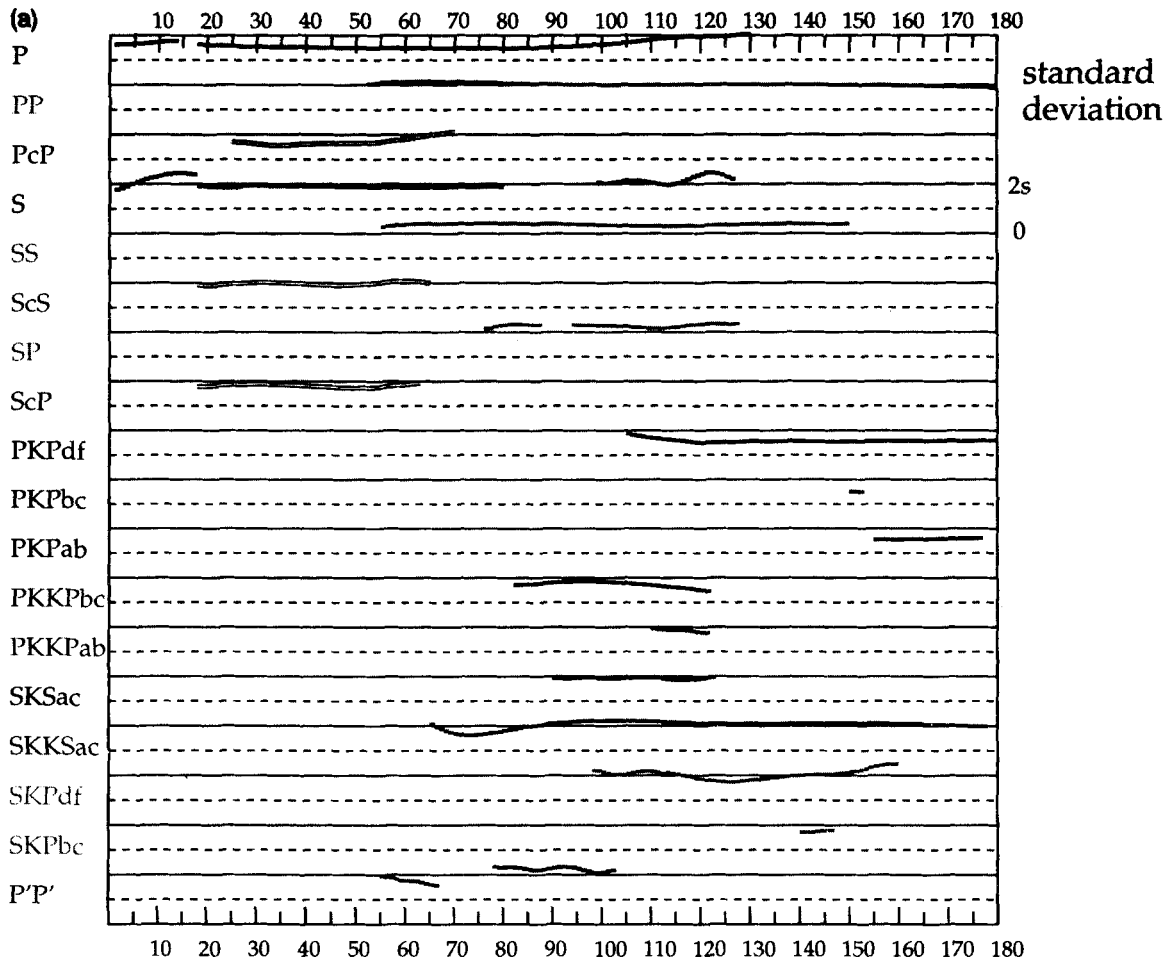
**Figure 3.** (a) Composite display of the standard deviation estimates from the construction of the smoothed empirical times for each of the branches shown in Fig. 2.

smoothed residual times which translate into undulations in the residual patterns.

The *iasp91* model and associated software provided the first computationally convenient system for multiphase traveltimes for the whole globe and have been employed in a wide variety of studies. However, the modified *pem* core used in the *iasp91* model is not adequate to explain all the properties of the core phases.

## 3 DEVELOPMENT OF A RADIAL VELOCITY MODEL

A convenient representation of the characteristics of a radial velocity model is to combine the traveltime residuals for the model with the information on the variance of the smoothed empirical times. This can be achieved by plotting the residual for each 1° cell normalized by the standard deviation estimate for that cell.

In Fig. 4(a) we display the residuals for *iasp91* in this normalized form. We once again use a composite plot so that the full range of phases can be displayed together; the width of the panel for each phase is now $\pm 1\sigma$ about the empirical times. For a comparison, in Fig. 4(b) we show the equivalent normalized residuals for the *sp6* model of Morelli & Dziewonski (1993). In contrast to *iasp91*, which had an

imposed core structure, *sp6* was derived by a linearized inversion process that included the *PKP* and *SKS* phases, and these phases are generally well represented. There are some deviations for the $PKP_{ab}$ branch, and Morelli & Dziewonski note that these *ab* branch residuals are difficult to remove with the parametrization employed (a cubic polynomial in radius in the outer core). The aim of Morelli & Dziewonski (1993) was to produce a close approach to a 'global average' model and they incorporated corrections for 3-D structure, which seem to be the origin of the significant deviations from the smoothed residual times for *P* waves beyond 80°. *S* shows a slight baseline offset but this is smaller than for *iasp91*. Although *sp6* provides a good representation of the main core phases, the fit to the less prominent phases is comparable to that of *iasp91*

In addition to the estimates of the seismic traveltimes, an important constraint on core structure (especially near the inner core boundary) is provided by the differential times between the various branches of *PKP*. With current high-quality digital records, such measurements can be made with high accuracy and are independent of the origin time of the source. We have made use of compilations of such differential times by Song & Helmberger (1995), Creager (1992) and McSweeney *et al.* (1995). The differential time residuals for the *PKP* phases in the *iasp91* and *sp6* models
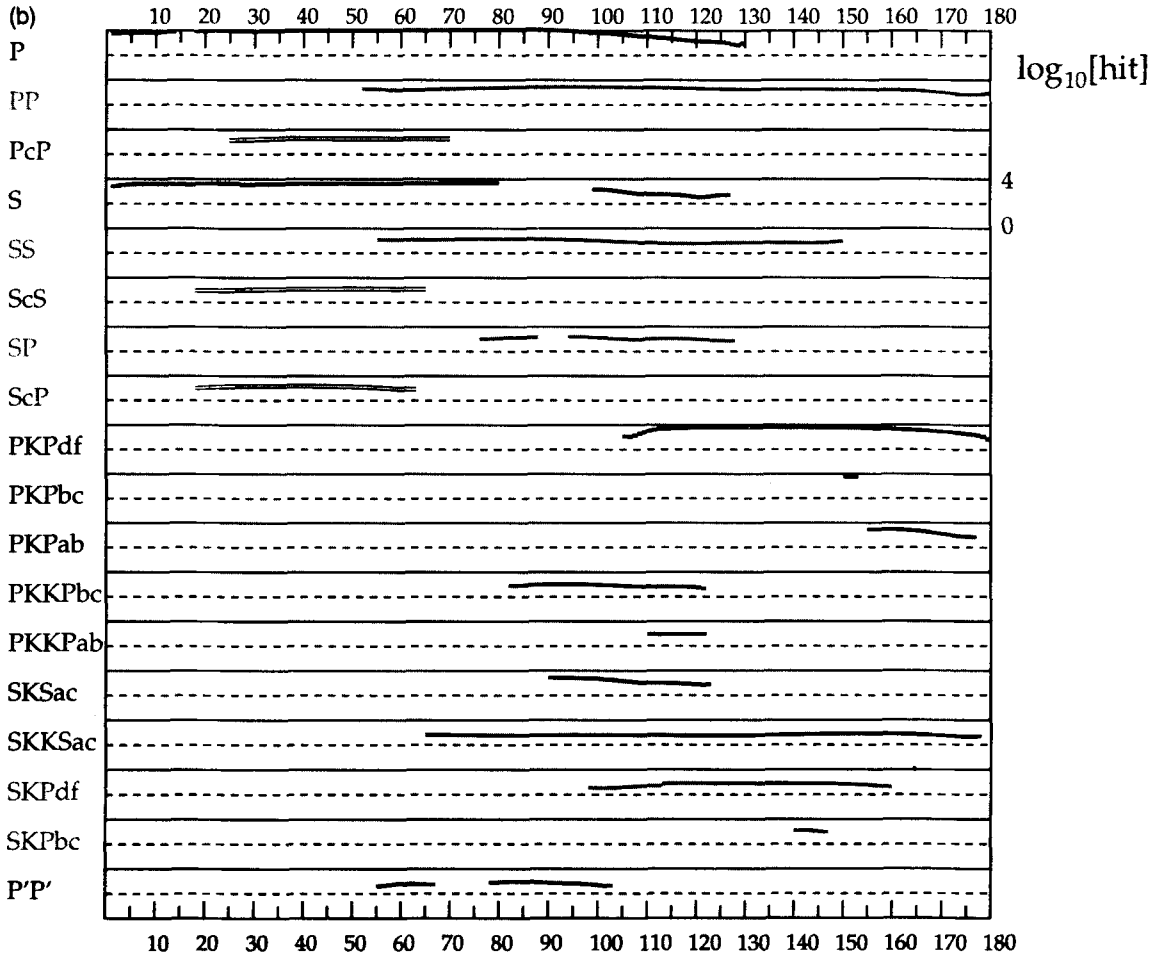
**Figure 3.** (b) Logarithmic display of the 'hit-count' for each 1° interval for each of the phase branches.

are summarized in Fig. 5. For *iasp91* the $ab - df$ differential times are quite well represented, but the trends of the $ab - bc$ and $bc - df$ times do not fit the observations. On the other hand, for *sp6* there is a distinct tilt in the $ab - df$ residuals at larger epicentral distances and an offset in the $bc - df$ residuals.

### 3.1 Measures of traveltime fit

The properties of the *iasp91* and *sp6* models provide a good deal of information to guide the construction of improved velocity models with particular emphasis on core structure. However, when we are working with such a wide range of seismic phases, we face an interesting problem as to the appropriate choice of criterion to provide a quantitative measure of the characteristics of the model. Rather than construct a single fit criterion, we found it advantageous to work with a number of measures of fit in which different aspects of the traveltimes are emphasized.

For each phase branch we construct an $L_2$ measure of fit between the smoothed empirical times and the predictions for a particular model. For example, for the $P$ phase we construct

$$\psi_P = \frac{1}{N_P}\left[\sum_{j=1}^{N_P}\left(\frac{(t_{\mathrm{obs}})_j - (t_{\mathrm{calc}})_j}{\sigma_j}\right)^2\right]^{1/2}, \tag{3.1.1}$$

where $N_P$ is the total number of 1° samples for the $P$ phase. Then, we use linear combinations of these individual phase measures to produce composite measures of fit encompassing a number of phases. A rather simple measure of overall performance is provided by the sum of the $\psi_{\mathrm{branch}}$ contributions for the 18 phase branches. The standard deviation estimates $\sigma_j$ are derived from the construction of the smoothed traveltime tables and do not include any assessment of systematic errors for later arrivals.

We have found it most effective to make use of weighted sums of the $\psi_{\mathrm{branch}}$ measures in which we try to give some measure of the significance of the contributions from different types of phases. The somewhat subjective set of weights $w_{\mathrm{branch}}$ (Table 1) are based on an assessment of the likely quality of phase picks, taking into account the expected amplitude of the arrivals and the coda of the preceding phases.

Two useful measures of traveltime fit are directed towards the major phases involving $P$ and $S$ propagation:

$$P1w = w_P\psi_P + w_{PcP}\psi_{PcP} + \sum w_{PKP}\psi_{PKP},$$
$$S1w = w_S\psi_S + w_{ScS}\psi_{ScS} + w_{SKS}\psi_{SKS}, \tag{3.1.2}$$

where the summation is taken over all the *PKP* branches. We can concentrate on the core by combining those phases
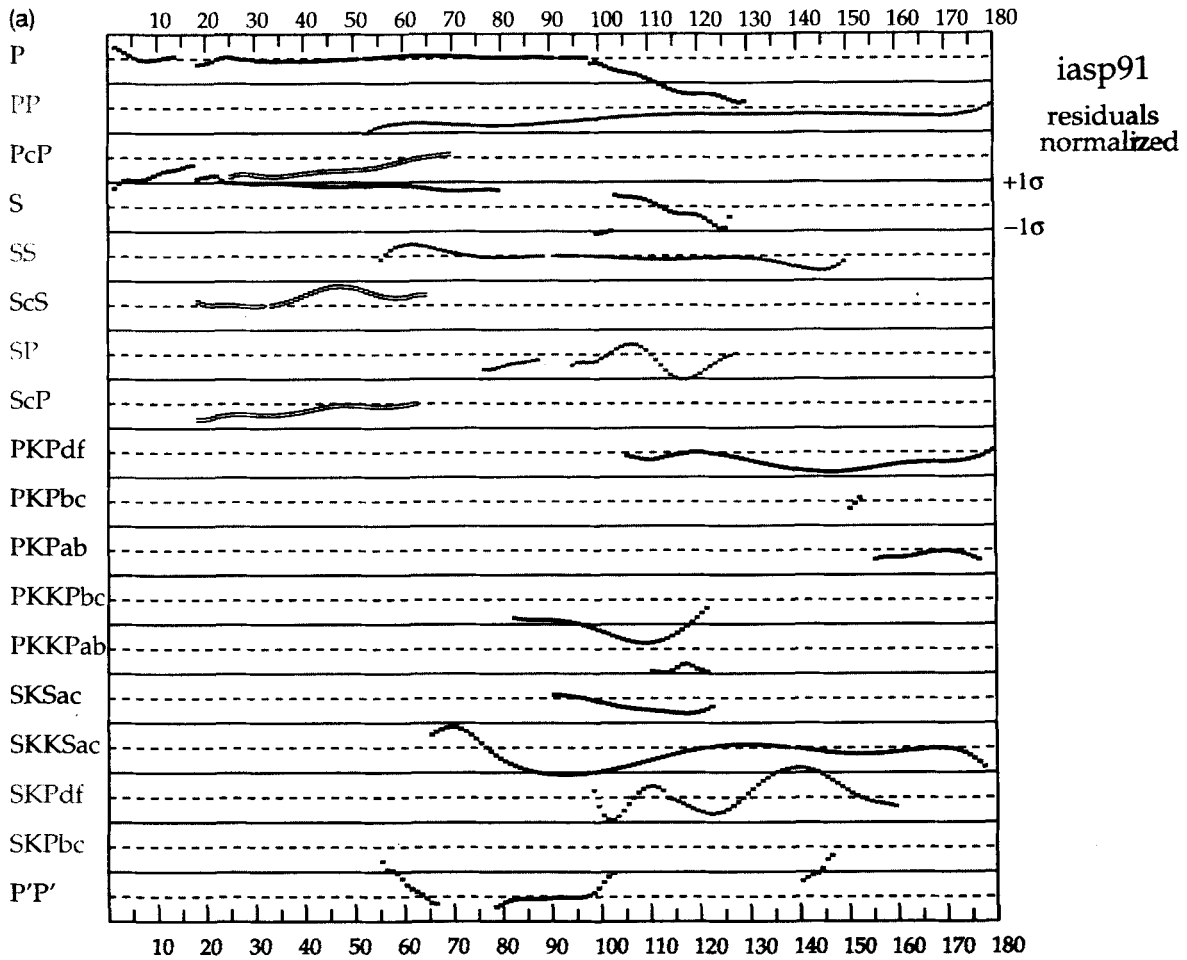
**Figure 4.** Composite display of the normalized residuals between the traveltimes predicted for radial velocity models and the smoothed empirical traveltimes. The residuals are normalized by the standard deviation estimates of Fig. 2. Velocity models: (a) *iasp91*, (b) *sp6*.

with solely mantle $P$ propagation:

$$CPw = \sum w_{PKP}\psi_{PKP} + \sum w_{PKKP}\psi_{PKKP} + w_{P'P'}\psi_{P'P'}, \quad (3.1.3)$$

or, alternatively, on phases involving $S$ waves in the mantle:

$$CSw = w_{SKS}\psi_{SKS} + w_{SKKS}\psi_{SKKS} + \sum w_{SKP}\psi_{SKP}, \quad (3.1.4)$$

We can combine all the main phases in a single measure:

$$A1w = P1w + S1w + w_{ScP}\psi_{ScP}, \quad (3.1.5)$$

or, in addition include core multiples and conversions:

$$A2w = A1w + \sum w_{PKKP}\psi_{PKKP} + w_{SKKS}\psi_{SKKS} + \sum w_{SKP}\psi_{SKP}. \quad (3.1.6)$$

A final measure is the weighted sum of all the misfits for all the branches:

$$ALw = \sum_{\text{branches}} w_{\text{branch}}\psi_{\text{branch}}. \quad (3.1.7)$$

This collection of misfit measures provides a useful assessment for any model. In addition, the relative size of the misfit measures for the different *PKP* branches frequently provides a guide to the differential time

behaviour. A tilt in the differential time residuals is likely to occur when one branch is fitted much more effectively than the others.

Both *iasp91* and *sp6* are based on the style of parametric representation employed for *prem* (Dziewonski & Anderson 1981). Although such a formulation is suitable for a linearized inverse scheme with a single misfit function, it is not as effective for adjusting models when multiple criteria are being used. The *iasp91* and *sp6* models below 660 km depth were therefore recast in terms of a sequence of linear gradients in radius with nodes approximately every 50 km, and this representation was used for all the other models.

### 3.2 Construction of a model

The first state in constructing a suitable model was to exploit the good $P$ behaviour of *iasp91* and remove the $S$ baseline shift by a slight adjustment in upper mantle structure. To improve the *PKP* residuals, the *sp6* core structure was used to create a new composite model *iasp93a*. The $S$ and *PKP* residuals are reduced as expected, but the misfit for *SKS* is noticeably increased (see Table 2). Also, the differential time behaviour corresponds directly to *sp6*.
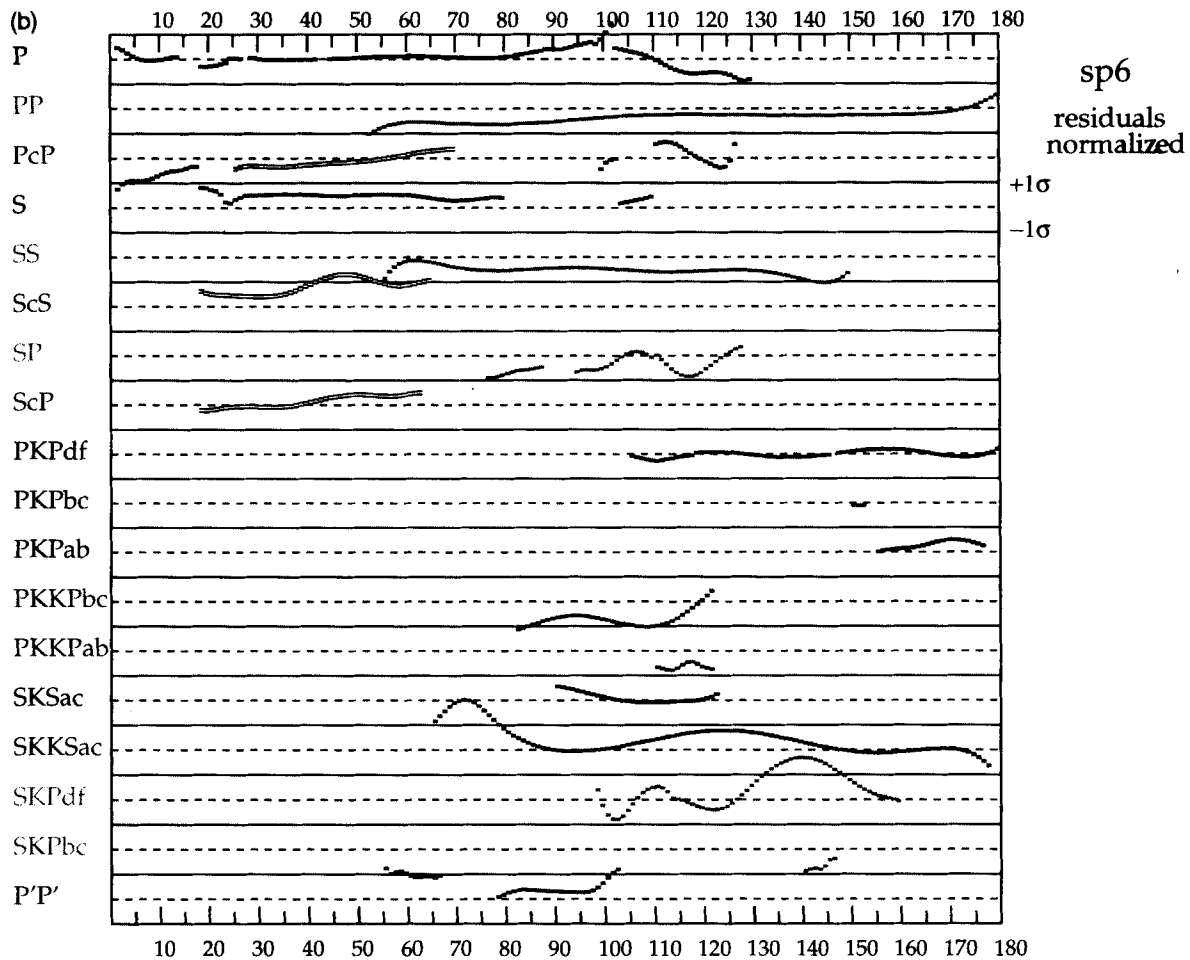
A further step was to attempt to reconcile the $P$ and $S$

**Figure 4.** (*Continued.*)

refracted phases from the mantle with the reflections from the core–mantle boundary *PcP*, *ScS* and *ScP*. This could be achieved by a slight modification in the *P* and *S* velocity distribution in the lower mantle together with a 0.5 km reduction in core radius from the *sp6* value to 3479.5 km. In order to reduce the *PcP* misfits, it was necessary to decrease the *P* velocity in the lowermost mantle below the *iasp91* value but not by as much as in *sp6*.

Once the fits to mantle phases were satisfactory, we could start modifying the core structure to give a good fit to the core phases. The primary guide to the core velocity distribution was *sp6*, but it proved necessary to modify the structure in the outer part of the core to meet the constraints imposed by *SKS* and *SKKS*. The changes to mantle *S* to improve the baseline fit tend to decrease the transit time for the *S* legs of the *SKS* path. In compensation, it proved necessary to decrease the *P* velocity in the outer part of the core from the values for *sp6*. With such a model, a good fit could be achieved to the *PKP* branches, but the match to the differential times was not really satisfactory.

Recently, both Song & Helmberger (1994) and Kaneshima *et al.* (1994) have suggested that the waveforms of *PKP* branches are best represented by models in which the velocity gradient is relatively low on either side of the boundary between the inner core and the outer core (ICB). There are some differences in the models proposed by Song

& Helmberger and Kaneshima *et al.*, which are probably related to the complications imposed by the anisotropy of the inner core. Time shifts of 2 s or more for *PKIKP* ($PKP_{df}$) can be imposed which depend on the orientation of the rays to the polar axis (see e.g. Shearer & Toy 1991).

In the context of radial, isotropic velocity models, the effect of anisotropy can be simulated via a change in the velocity contrast at the ICB. The smoothed empirical times will include a fair amount of geographical averaging, and we have found that we can obtain a good fit to all the *PKP* branches with a structure similar to that proposed by Song & Helmberger (1994). Such a model also has a satisfactory pattern of differential times.

A large number of models were tested during this construction process in order to assess the trade-offs between different aspects of the velocity structure. For each model, a full calculation of the traveltime residuals was carried out for all phases, and for promising models differential-time residual plots were also prepared.

The model *ak135* which is the product of this procedure provides a good fit to a wide range of phases, as can be seen from the normalized residual plot in Fig. 6(a) and the compilation of misfit measures in Table 2. The *P* residuals are small throughout. The baseline and trend of *S* is well presented. Compared with *iasp91* and *sp6*, the fits to the reflected phases *ScS* and *ScP* are improved. *PcP* is nearly as
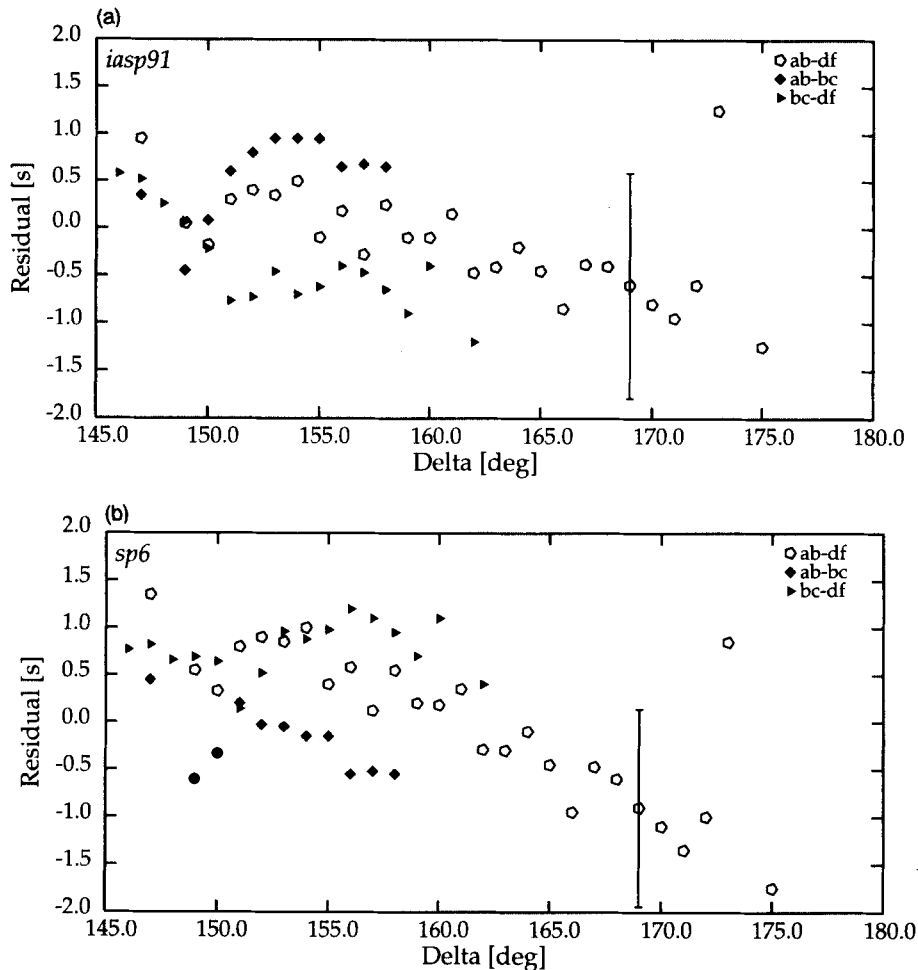
**Figure 5.** Differential time residuals for *PKP* branches determined from GDSN records compared with model predictions. Medians over one degree cells are shown for each branch; the relatively large scatter for larger distances is indicated by displaying the spread in the median at 169°. Velocity models: (a) *iasp91*, (b) *sp6*.

well matched as for *sp6*, with a better match for *P*. The fit to the phases that have undergone surface reflections (*PP*, *SS*, *SP*) is not as good as for the *P* and *S* phases. Such surface-reflected phases tend to be of lower frequency than the direct phases and also their waveforms will be phase-shifted by 90° from the original source pulse. As a result, we can expect that the picks could be late, which is consistent with the patterns of negative residuals.

The main core phases are fitted well with *ak135*. With the exception of part of *P'P'* and a small distance range for *SKP*, all the other residuals for the core phases are less than the estimated standard deviations σ from the empirical traveltime set. The waveforms for the *SKKS* and *PKKP* phases should both experience a 90° phase shift associated with the internal reflection at the underside of the core–mantle boundary. Since there is no way of knowing the procedures used by the very large number of stations that report to the ISC, we have been forced to match the empirical traveltimes. Differences in structure in the outermost core between *ak135* and the models discussed by Garnero, Helmberger & Grand (1993) based on *S3KS-SKKS* and *S4KS-S3KS* differential traveltimes measured by waveform correlation techniques are quite likely to be

associated with the influence of the phase shift and the high level of heterogeneity at the base of the mantle.

The behaviour of the *ak135* model is compared with *iasp91*, *sp6* and *iasp93a* in Table 2. In addition, we include the model *ak303* derived during the course of this work which gives a slightly better fit to some of the core phases at the expense of a less good fit to the *PKP* branches. In Table 2(a) we compare the misfit measures for each of the 18 phase branches, and in Table 2(b) we include the range of composite measures introduced in Section 3.1.

Table 2 shows clearly the improvement in fit for both major and minor phases achieved in the process of model construction. The *iasp93a* model is an improvement on *iasp91*, and has achieved an improved result for *S* compared with *sp6*. The model *sp6* has better fit for each of the composite measures than *iasp91*, but the modifications made to produce *ak135* have made a significant improvement to each of the composite measures and to most of the individual phases, except those reflected at the free surface (*PP*, *SS*, *SP*, *P'P'*).

The differential time behaviour for the *PKP* branches for model *ak135* is displayed in Fig. 6(b). The change of structure near the inner core boundary has had the effect of
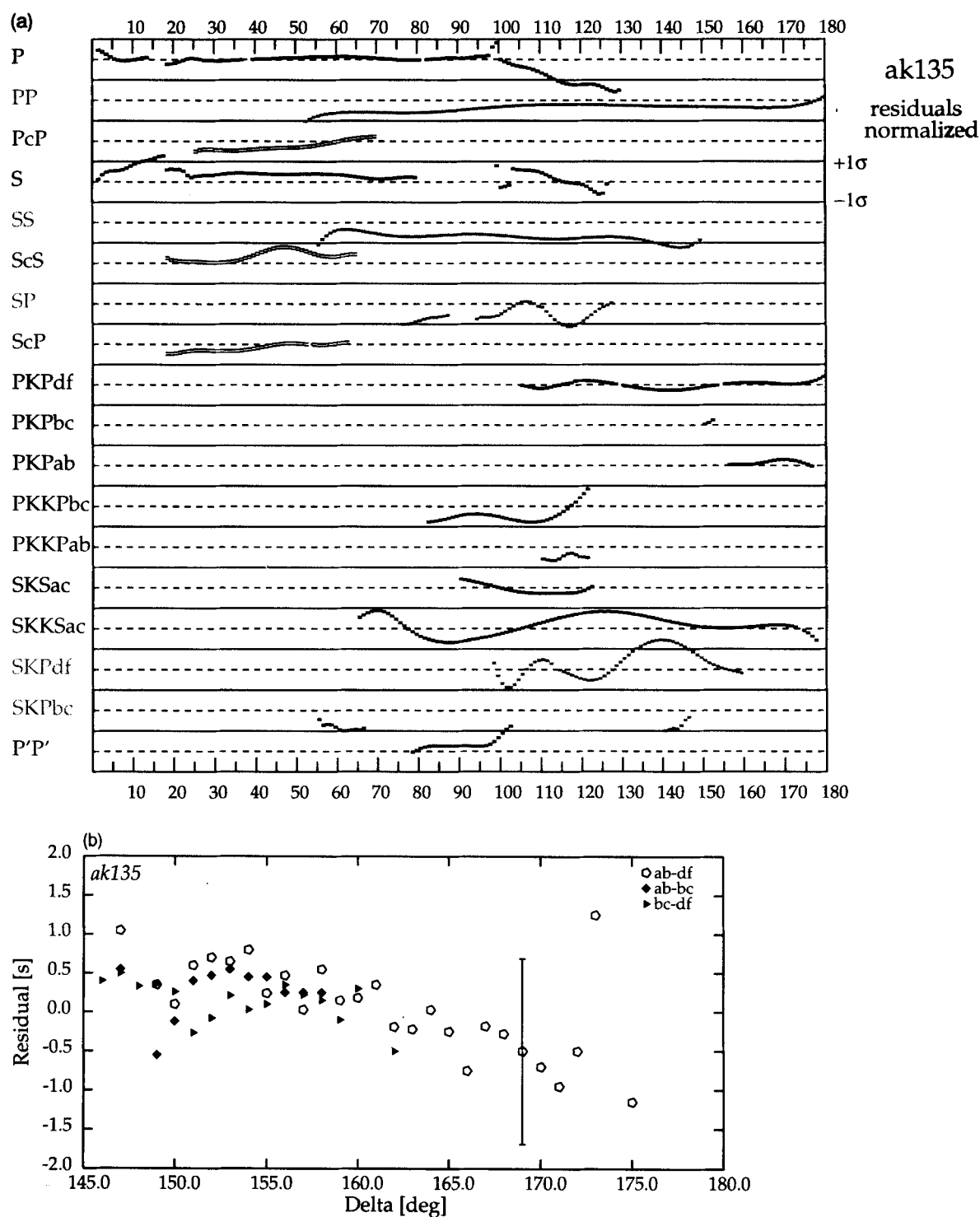
**Figure 6.** (a) Composite display of the normalized residuals between the traveltimes predicted for model *ak135* and the smoothed empirical traveltimes. (b) Differential traveltime residuals for model *ak135*, as in Fig. 5, the medians over one degree cells are displayed for each branch.

eliminating the tilts in the residual patterns and the agreement between the predictions from the radial velocity profile and the measurements from the digital records is generally good.

Figure 7 displays the models *iasp91*, *iasp93a*, *ak303* and *ak135* relative to *sp6* so that the differences can be seen. The differences between *ak303* and *ak135* are slight and lie mostly in the lower part of the mantle and in a slightly different radius for the inner core. Except for near the core–mantle boundary and the inner-core boundary, the differences between *ak135* and *sp6* are smaller than $0.02\ \mathrm{km\,s^{-1}}$. In the lower mantle, the $P$ and $S$ are generally slightly closer to *iasp91* than to *sp6*, but in most of the outer core *ak135* follows *sp6* quite closely. The relatively small

**Table 2.** Misfit measures.

| Phase | iasp91 | sp6 | iasp93a | ak303 | ak135 |
|-------|--------|-----|---------|-------|-------|
| P | 0.005 | 0.045 | 0.005 | 0.013 | 0.008 |
| PP | 0.210 | 0.172 | 0.213 | 0.160 | 0.176 |
| PcP | 0.276 | 0.066 | 0.155 | 0.109 | 0.104 |
| S | 0.698 | 0.430 | 0.120 | 0.139 | 0.119 |
| SS | 0.056 | 0.333 | 0.553 | 0.611 | 0.555 |
| ScS | 0.197 | 0.820 | 0.073 | 0.182 | 0.217 |
| SP | 0.247 | 0.284 | 0.566 | 0.459 | 0.434 |
| ScP | 0.085 | 0.085 | 0.109 | 0.050 | 0.038 |
| PKPdf | 0.218 | 0.016 | 0.058 | 0.040 | 0.023 |
| PKPbc | 0.039 | 0.010 | 0.111 | 0.069 | 0.026 |
| PKPab | 0.052 | 0.106 | 0.144 | 0.061 | 0.029 |
| PKKPbc | 1.496 | 0.594 | 0.886 | 0.255 | 0.329 |
| PKKPab | 0.692 | 0.430 | 1.144 | 0.189 | 0.273 |
| SKSac | 0.156 | 0.051 | 0.328 | 0.064 | 0.056 |
| SKKSac | 0.287 | 0.481 | 0.272 | 0.248 | 0.236 |
| SKPdf | 0.385 | 0.703 | 0.534 | 0.497 | 0.524 |
| SKPbc | 0.991 | 0.486 | 1.288 | 0.585 | 0.606 |
| P'P' | 0.238 | 0.475 | 0.221 | 0.637 | 0.599 |

| Measure | iasp91 | sp6 | iasp93a | ak303 | ak135 |
|---------|--------|-----|---------|-------|-------|
| P1w | 1.813 | 0.885 | 1.587 | 0.963 | 0.560 |
| S1w | 2.447 | 2.161 | 0.761 | 0.663 | 0.630 |
| CPw | 4.756 | 2.539 | 4.518 | 1.983 | 1.814 |
| CSw | 2.131 | 1.823 | 3.078 | 1.522 | 1.534 |
| A1w | 4.430 | 3.216 | 2.566 | 1.726 | 1.266 |
| A2w | 9.518 | 6.662 | 7.841 | 3.846 | 3.653 |
| ALw | 10.375 | 8.012 | 9.501 | 5.793 | 5.505 |

changes in velocity have, however, markedly improved the level of fit that can be achieved to the empirical traveltimes.

## 4 RESOLUTION OF MANTLE AND CORE STRUCTURE

Once we have constructed a model such as *ak135*, an important question which needs to be answered is the reliability of the proposed structure. To avoid restrictive assumptions based on linearization, we have developed a non-linear procedure to scan a broad range of models around the *ak135* reference.

We have established a set of velocity bounds about *ak135*, for both P and S wavespeeds. As illustrated in Fig. 8, we have allowed up to $\pm 0.02$ km s$^{-1}$ variation in the velocities between 760 and 2500 km, and have then expanded the bounds in the lowermost mantle to reach $\pm 0.04$ km s$^{-1}$ at the core–mantle boundary. The bounds for the P-wave velocity in the core were also taken as $\pm 0.04$ km s$^{-1}$. These bounds are broad enough to encompass the differences between *ak135* and the *iasp91*, *sp6* models. For most of the earth the *prem* model lies within these bounds.

In order to explore the range of suitable models, we have drawn a set of models from a uniform random population, subject to the velocity bound constraints and the requirement that velocity gradients lie within 25 per cent of the value for *ak135*. With the linear gradient representation for the velocity model, we have used a velocity discretization of 0.009 km s$^{-1}$ for P and 0.006 km s$^{-1}$ for S. A set of 5000 random models spans the full velocity bounds for both P and S velocities.

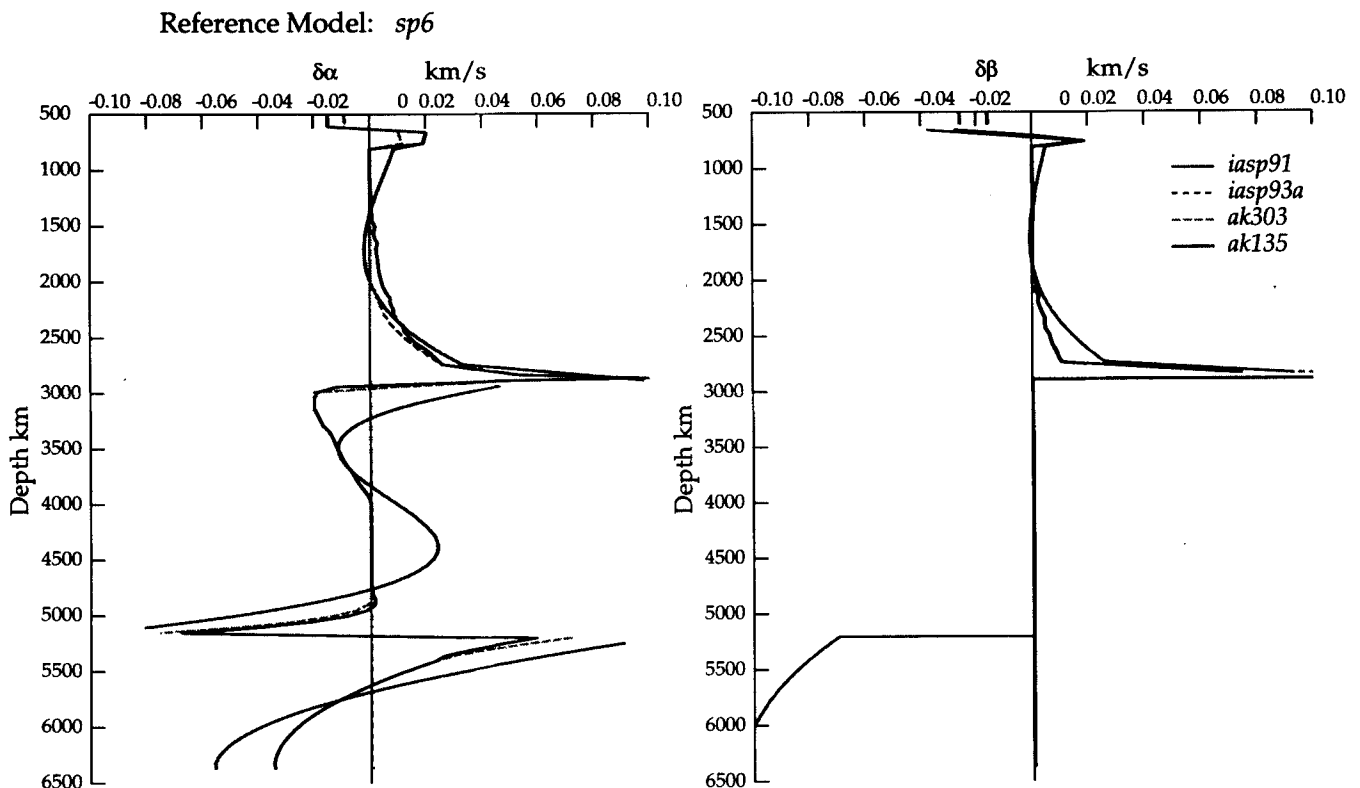### Reference Model: *sp6*



**Figure 7.** Relative velocity display of models compared with *sp6*.
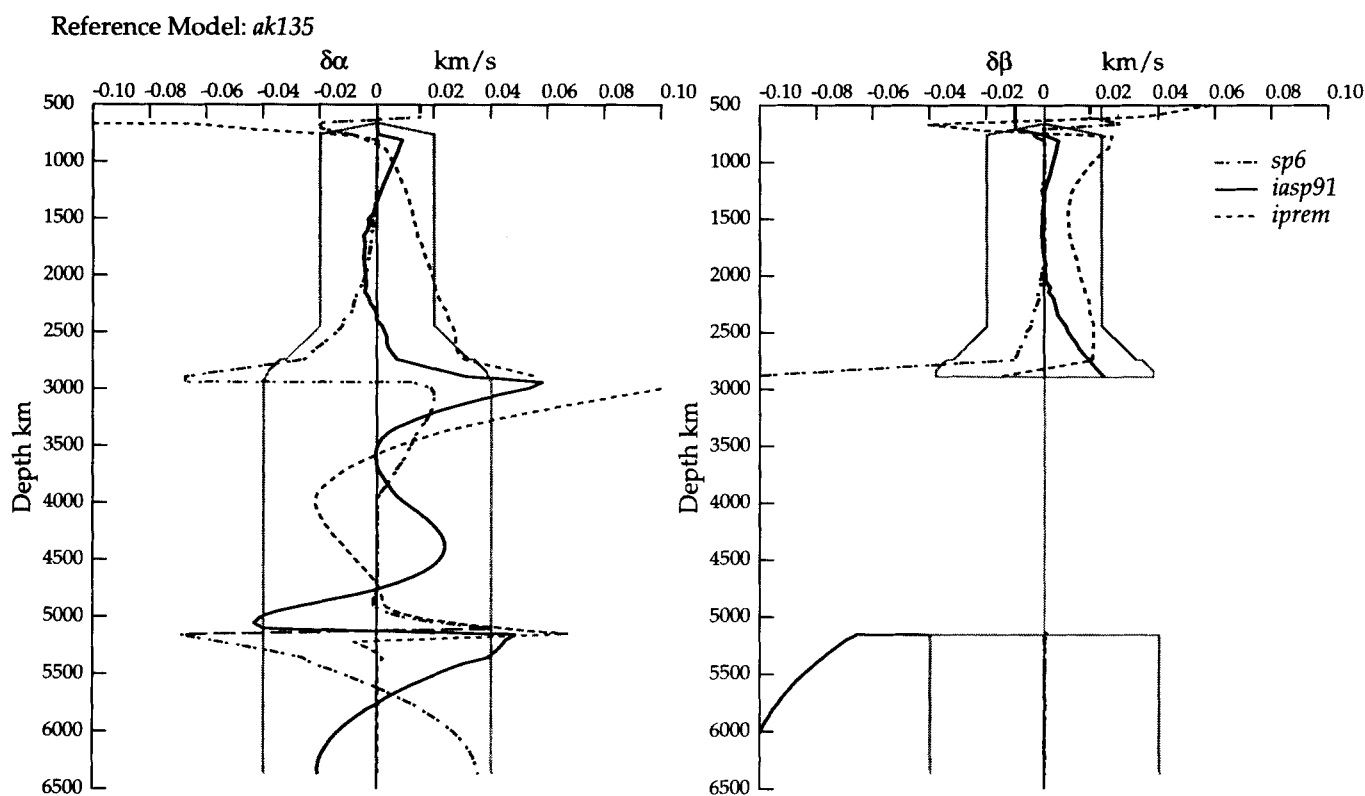
# Reference Model: *ak135*



**Figure 8.** Velocity bounds around model *ak135* compared to other velocity models.

For each of the 5000 random models, a full representation of the traveltimes was made for all 18 phase branches and then compared with the smoothed empirical times. The misfit measures for all phases were stored for each model. In order to avoid too restrictive a treatment of structure in the neighbourhood of the ICB, we added 50 models drawn from the search procedure described in the previous section; these models span the range of styles considered and include the *iasp91*, *sp6* and *iasp93a* models.

We then applied the range of composite measures of fit introduced in Section 3.1 to the augmented set of 5050 models of lower mantle and core structure. For each measure of traveltime misfit we extracted the best 100 models based on this particular misfit criterion. A good measure of those aspects of the velocity structure that are favoured by this particular combination of data is provided by a density plot of model count across the top 100 models (see Figs 9–11).

In Fig. 9 we compare the behaviour based on the measures *P1w*, *S1w* which are keyed to the major *P* or *S* phases. We have superimposed on the pixel plots the best-fitting model for each fit criterion as a white line. Because the radial node interval is quite fine (~50 km) it is possible to develop somewhat rough structure, especially where model constraints are weak.

For the *P1w* measure, the best-fitting model came from the model construction sequence. In the mantle the general trend of the best 100 models for *P1w* is close to the *ak135* reference with some tendency to slightly higher velocities. For the core, the weak constraints provided on the upper part of the outer core are in sharp contrast to the model

concentration in the zone where *PKP* is significant; some variety in inner-core structure is apparent. By contrast, the *S*-wave models that provide the best fit to the *S1w* measure give a clear preferred trend except in the lower most mantle.

On occasions, the different composite measures of misfit can suggest different styles of structure. In Fig. 10 we compare the results for the measures *CPw* and *CSw* based on the core phases. We need to recall that the *P* waves entering the core do not sample the top 1000 km, and so the scatter in this range for the *CPw* measure plot is not surprising. There is a greater constraint for the waves with *S* legs in the mantle, and so the best models with the *CSw* measure are more consistent in the outermost core. However, when we look in the middle core, where there should be some resolution from both classes of arrival, we note that the best-fitting models for the *CPw* measure favour higher velocities than in *ak135*, whereas those for the *CSw* measure concentrate on slightly lower velocities than in *ak135*. This example illustrates the complex balance between competing classes of information which have to be reconciled to produce a suitable reference model.

The various measures of fit based on the widest range of phases yield a concentration of model profiles close to the *ak135* reference. In Fig. 11, we display the *P* and *S* velocity distributions for measure *A2w*, which are very similar to those for the *A1w* and *ALw* measures. In this case, the best-fitting model is the reference, but for *A1w*, and *ALw* somewhat rougher models give a marginally better fit. The combination of core phases with both *P* and *S* legs in the mantle has enhanced the main trend in the velocities, but significant scatter is apparent among the 100 best-fitting
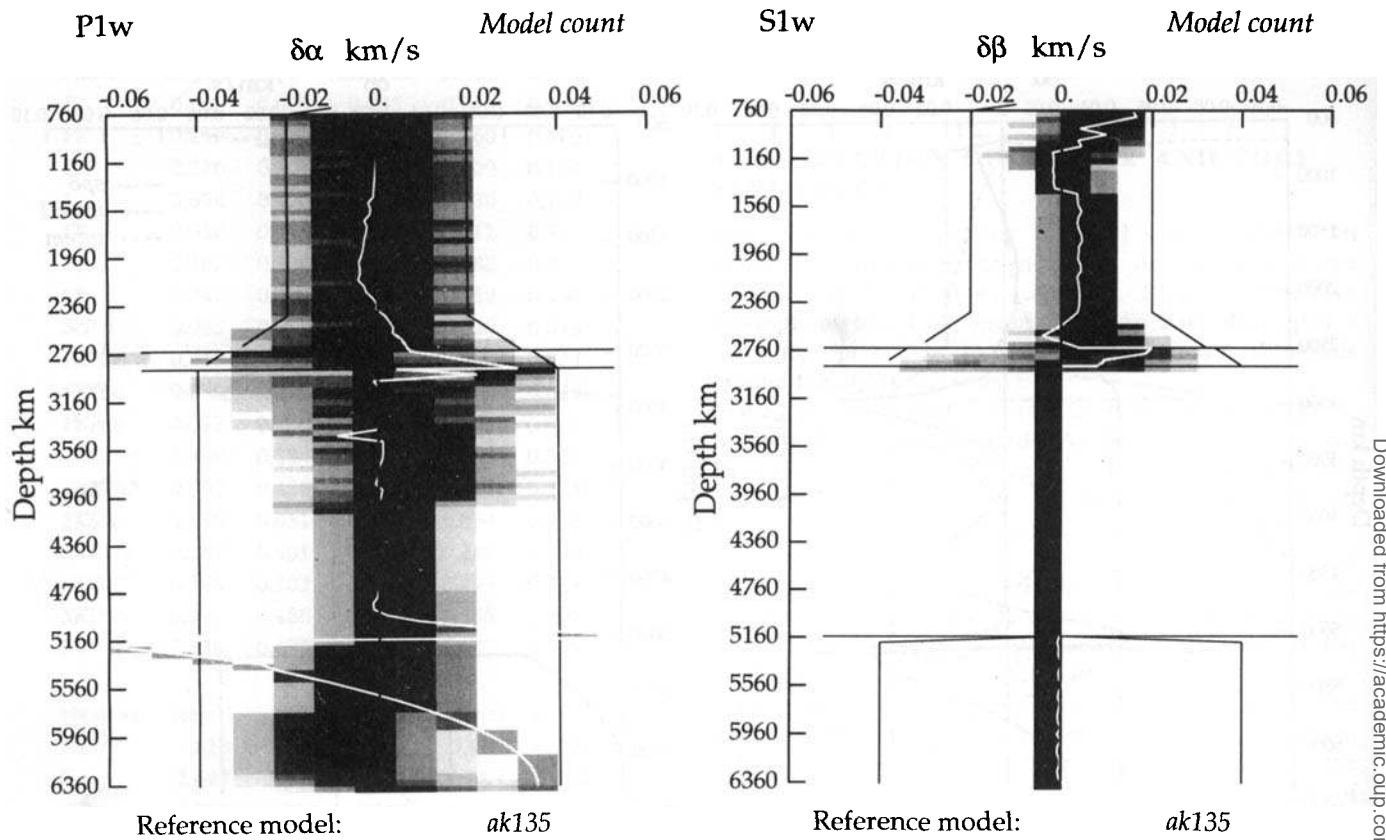
**Figure 9.** Model density plots for the best 100 models for misfit measures *P1w* (*P* wavespeeds) and *S1w* (*S* wavespeeds).
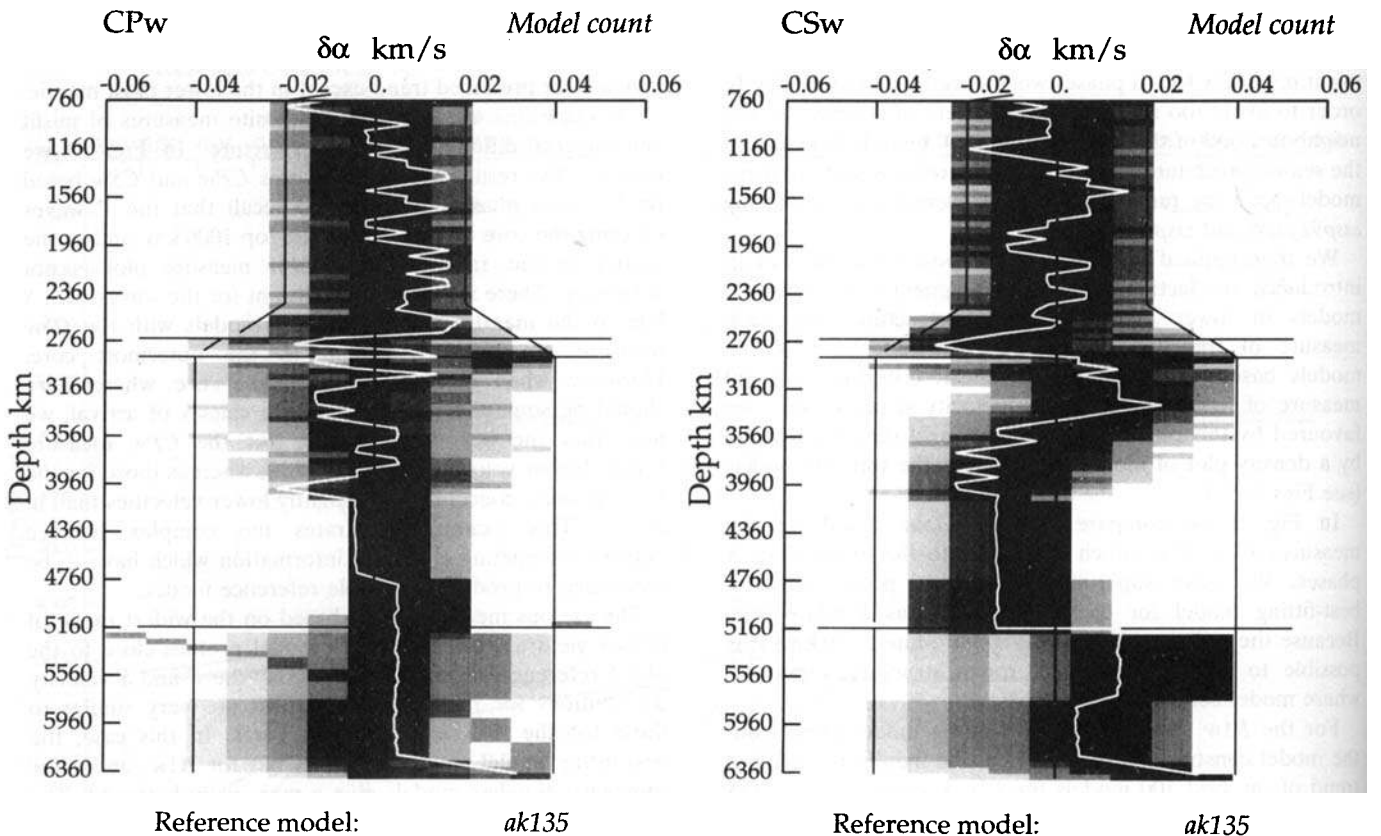


**Figure 10.** Model density plots for the best 100 *P* wavespeed models for misfit measures *CPw* and *CSw*.
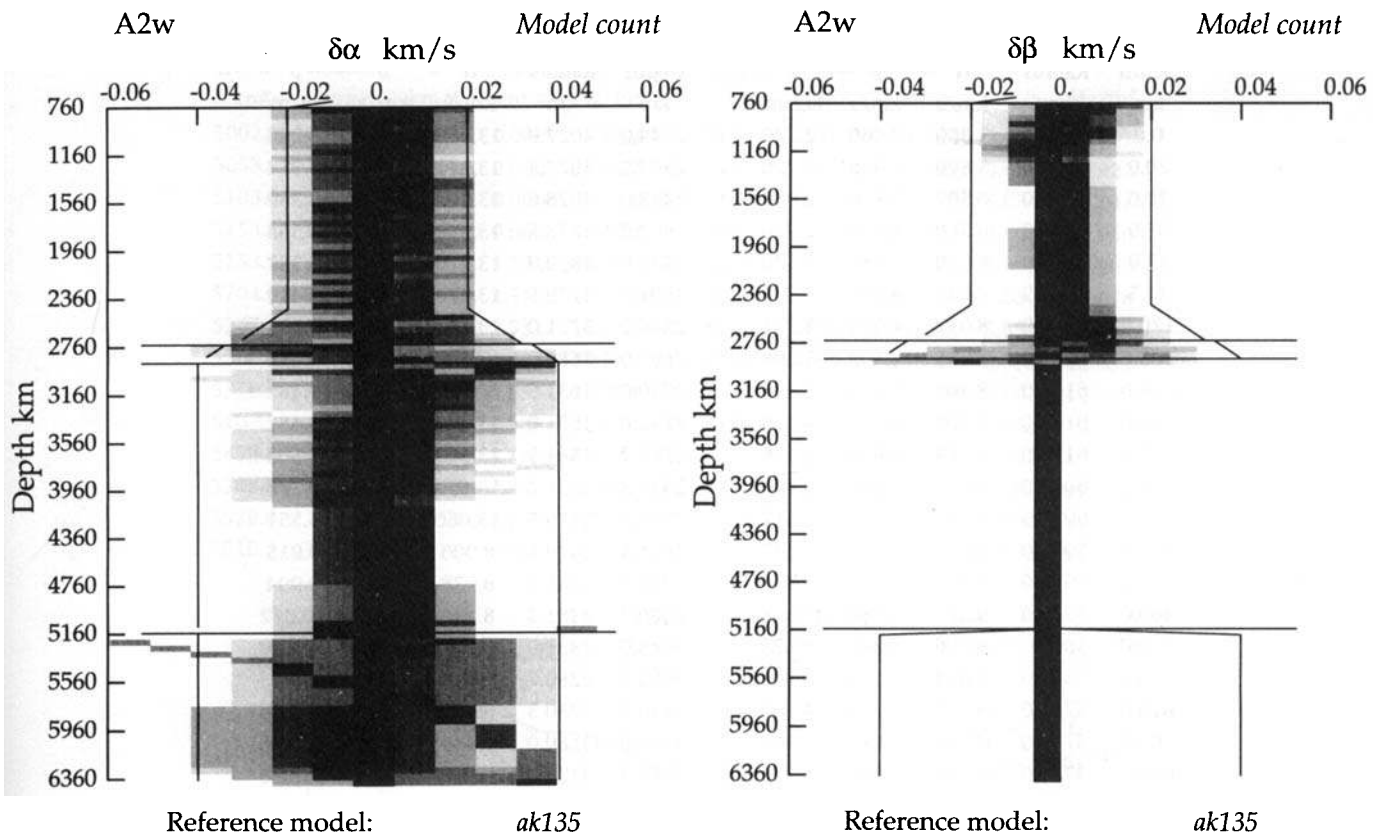
**Figure 11.** Model density plots for the best 100 models for both *P* and *S* wavespeeds for the misfit measure *A2w*.

models. The model density pictures suggest that there is a possibility that *ak135* velocities may be a little too low in a thin zone just below the core–mantle boundary for optimum fit to the smoothed empirical times. Except in the inner core and the D″ region, we can constrain the velocities within $\pm 0.01 \, \text{km s}^{-1}$ for *P* and *S* with a reasonable level of confidence.

## 5 DISCUSSION

In the previous section we have seen that the model *ak135* is an effective model which provides a good representation of the full set of smoothed empirical traveltimes. The adjustments that have had to be made to the previous body-wave models *iasp91* and *sp6* are not very large, except at the inner-core boundary.

Since the smoothed empirical times were derived using events relocated with the *P* times for *iasp91*, we have undertaken a further check on the model. We have re-extracted smoothed empirical times from the selected events after relocation using the *ak135* model. The residual patterns are visually indistinguishable from those presented in Fig. 6(a).

We stress that model *ak135* is designed to represent the smoothed empirical traveltimes, and so should be very suitable for predicting the arrival times of a wide variety of seismic phases for use in event location or phase association

procedures. We have to be cautious about direct interpretation of *ak135* as a full representation of seismic velocities in the Earth. Resolution of structure in some zones remains weak, notably at the base of the mantle and in the uppermost core.

The velocity profile for *ak135* is presented in Table 3 and a comparison of the model with *iasp91*, *sp6* and *prem* is displayed in Fig. 12. The relative velocities of these models with *ak135* as a reference are also displayed in Fig. 8. There is a close concordance between *ak135*, *iasp91* and *prem* in the middle mantle. In the lower part of the mantle, *ak135* is slightly faster than *sp6* but slower than *iasp91* or *prem*. The velocity gradients in D″ for both *P* and *S* are low for *ak135*, but not negative as adopted in *sp6*. The strong lateral heterogeneity in this region means that, as in the upper mantle, the structure is representative and is consistent with the range of traveltime constraints. However, the *ak135* model may well not be consistent with the local properties of D″.

The model *ak135* has relatively low velocities at the top of the core, but is slightly faster than *prem* in the middle of the outer core. As we have noted above, the main difference arises near the inner-core boundary, where *ak135* has reduced velocity gradients. The range of velocity jumps at the ICB displayed by the various models should cover the apparent variations induced by the presence of anisotropy in the inner core.

**Table 3.** Model *ak135*.

| Depth km | Radius km | $\alpha$ km/s | $\beta$ km/s | $\rho$ Mg/m$^3$ | Depth km | Radius km | $\alpha$ km/s | $\beta$ km/s | $\rho$ Mg/m$^3$ |
|---|---|---|---|---|---|---|---|---|---|
| 0.0 | 6371.0 | 5.800 | 3.460 | 2.720 | 2344.0 | 4027.0 | 13.189 | 7.072 | 5.290 |
| 20.0 | 6351.0 | 5.800 | 3.460 | 2.720 | 2393.5 | 3977.5 | 13.247 | 7.093 | 5.314 |
| 20.0 | 6351.0 | 6.500 | 3.850 | 2.920 | 2443.0 | 3928.0 | 13.302 | 7.114 | 5.339 |
| 35.0 | 6336.0 | 6.500 | 3.850 | 2.920 | 2492.5 | 3878.5 | 13.358 | 7.137 | 5.363 |
| 35.0 | 6336.0 | 8.040 | 4.480 | 3.320 | 2542.0 | 3829.0 | 13.416 | 7.159 | 5.387 |
| 77.5 | 6293.5 | 8.045 | 4.490 | 3.345 | 2591.5 | 3779.5 | 13.474 | 7.181 | 5.411 |
| 120.0 | 6251.0 | 8.050 | 4.500 | 3.371 | 2640.0 | 3731.0 | 13.531 | 7.203 | 5.435 |
| 165.0 | 6206.0 | 8.175 | 4.509 | 3.398 | 2690.0 | 3681.0 | 13.590 | 7.226 | 5.458 |
| 210.0 | 6161.0 | 8.300 | 4.518 | 3.426 | 2740.0 | 3631.0 | 13.649 | 7.249 | 5.482 |
| 210.0 | 6161.0 | 8.300 | 4.523 | 3.426 | 2740.0 | 3631.0 | 13.649 | 7.249 | 5.482 |
| 260.0 | 6111.0 | 8.483 | 4.609 | 3.456 | 2789.7 | 3581.3 | 13.653 | 7.260 | 5.505 |
| 310.0 | 6061.0 | 8.665 | 4.696 | 3.486 | 2839.3 | 3531.7 | 13.657 | 7.270 | 5.528 |
| 360.0 | 6011.0 | 8.847 | 4.783 | 3.517 | 2891.5 | 3479.5 | 13.660 | 7.281 | 5.551 |
| 410.0 | 5961.0 | 9.030 | 4.870 | 3.547 | 2891.5 | 3479.5 | 8.000 | 0.000 | 9.915 |
| 410.0 | 5961.0 | 9.360 | 5.080 | 3.756 | 2939.3 | 3431.7 | 8.038 | 0.000 | 9.994 |
| 460.0 | 5911.0 | 9.528 | 5.186 | 3.818 | 2989.7 | 3381.3 | 8.128 | 0.000 | 10.072 |
| 510.0 | 5861.0 | 9.696 | 5.292 | 3.879 | 3040.0 | 3331.0 | 8.221 | 0.000 | 10.149 |
| 560.0 | 5811.0 | 9.864 | 5.398 | 3.941 | 3090.3 | 3280.7 | 8.312 | 0.000 | 10.223 |
| 610.0 | 5761.0 | 10.032 | 5.504 | 4.003 | 3140.7 | 3230.3 | 8.400 | 0.000 | 10.296 |
| 660.0 | 5711.0 | 10.200 | 5.610 | 4.065 | 3191.0 | 3180.0 | 8.486 | 0.000 | 10.368 |
| 660.0 | 5711.0 | 10.790 | 5.960 | 4.371 | 3241.3 | 3129.7 | 8.569 | 0.000 | 10.438 |
| 710.0 | 5661.0 | 10.923 | 6.090 | 4.401 | 3291.6 | 3079.4 | 8.650 | 0.000 | 10.506 |
| 760.0 | 5611.0 | 11.056 | 6.209 | 4.431 | 3342.0 | 3029.0 | 8.728 | 0.000 | 10.573 |
| 809.5 | 5561.5 | 11.135 | 6.243 | 4.460 | 3392.3 | 2978.7 | 8.804 | 0.000 | 10.639 |
| 859.0 | 5512.0 | 11.222 | 6.280 | 4.489 | 3442.6 | 2928.4 | 8.876 | 0.000 | 10.702 |
| 908.5 | 5462.5 | 11.307 | 6.316 | 4.517 | 3493.0 | 2878.0 | 8.946 | 0.000 | 10.765 |
| 958.0 | 5413.0 | 11.390 | 6.351 | 4.546 | 3543.3 | 2827.7 | 9.014 | 0.000 | 10.826 |
| 1007.5 | 5363.5 | 11.470 | 6.385 | 4.574 | 3593.6 | 2777.4 | 9.079 | 0.000 | 10.885 |
| 1057.0 | 5314.0 | 11.550 | 6.419 | 4.603 | 3644.0 | 2727.0 | 9.143 | 0.000 | 10.943 |
| 1106.5 | 5264.5 | 11.627 | 6.451 | 4.631 | 3694.3 | 2676.7 | 9.204 | 0.000 | 11.000 |
| 1156.0 | 5215.0 | 11.703 | 6.483 | 4.659 | 3744.6 | 2626.4 | 9.263 | 0.000 | 11.056 |
| 1205.5 | 5165.5 | 11.777 | 6.514 | 4.687 | 3795.0 | 2576.0 | 9.321 | 0.000 | 11.109 |
| 1255.0 | 5116.0 | 11.849 | 6.544 | 4.715 | 3845.3 | 2525.7 | 9.376 | 0.000 | 11.162 |
| 1304.5 | 5066.5 | 11.920 | 6.573 | 4.742 | 3895.6 | 2475.4 | 9.430 | 0.000 | 11.214 |
| 1354.0 | 5017.0 | 11.990 | 6.601 | 4.770 | 3945.9 | 2425.1 | 9.481 | 0.000 | 11.264 |
| 1403.5 | 4967.5 | 12.058 | 6.628 | 4.797 | 3996.3 | 2374.7 | 9.531 | 0.000 | 11.313 |
| 1453.0 | 4918.0 | 12.125 | 6.655 | 4.825 | 4046.6 | 2324.4 | 9.578 | 0.000 | 11.360 |
| 1502.5 | 4868.5 | 12.191 | 6.681 | 4.852 | 4097.0 | 2274.0 | 9.623 | 0.000 | 11.407 |
| 1552.0 | 4819.0 | 12.255 | 6.707 | 4.878 | 4147.3 | 2223.7 | 9.667 | 0.000 | 11.452 |
| 1601.5 | 4769.5 | 12.318 | 6.733 | 4.905 | 4197.6 | 2173.4 | 9.710 | 0.000 | 11.496 |
| 1651.0 | 4720.0 | 12.382 | 6.757 | 4.932 | 4247.9 | 2123.1 | 9.751 | 0.000 | 11.539 |
| 1700.5 | 4670.5 | 12.443 | 6.781 | 4.958 | 4298.3 | 2072.7 | 9.791 | 0.000 | 11.581 |
| 1750.0 | 4621.0 | 12.503 | 6.805 | 4.985 | 4348.6 | 2022.4 | 9.830 | 0.000 | 11.622 |
| 1799.5 | 4571.5 | 12.563 | 6.829 | 5.011 | 4398.9 | 1972.1 | 9.868 | 0.000 | 11.661 |
| 1849.0 | 4522.0 | 12.622 | 6.852 | 5.037 | 4449.3 | 1921.7 | 9.905 | 0.000 | 11.700 |
| 1898.5 | 4472.5 | 12.680 | 6.874 | 5.063 | 4499.6 | 1871.4 | 9.941 | 0.000 | 11.737 |
| 1948.0 | 4423.0 | 12.738 | 6.897 | 5.089 | 4549.9 | 1821.1 | 9.976 | 0.000 | 11.774 |
| 1997.5 | 4373.5 | 12.796 | 6.919 | 5.114 | 4600.3 | 1770.7 | 10.010 | 0.000 | 11.809 |
| 2047.0 | 4324.0 | 12.853 | 6.942 | 5.140 | 4650.6 | 1720.4 | 10.044 | 0.000 | 11.844 |
| 2096.5 | 4274.5 | 12.910 | 6.963 | 5.165 | 4700.9 | 1670.1 | 10.077 | 0.000 | 11.877 |
| 2146.0 | 4225.0 | 12.967 | 6.985 | 5.190 | 4801.6 | 1569.4 | 10.142 | 0.000 | 11.941 |
| 2195.5 | 4175.5 | 13.022 | 7.006 | 5.215 | 4851.9 | 1519.1 | 10.174 | 0.000 | 11.972 |
| 2245.0 | 4126.0 | 13.078 | 7.028 | 5.240 | 4902.2 | 1468.8 | 10.205 | 0.000 | 12.000 |
| 2294.5 | 4076.5 | 13.134 | 7.050 | 5.265 | 4952.6 | 1418.4 | 10.233 | 0.000 | 12.031 |

**Table 3.** (*Continued.*)

| Depth km | Radius km | α km/s | β km/s | ρ Mg/m³ | Depth km | Radius km | α km/s | β km/s | ρ Mg/m³ |
|---|---|---|---|---|---|---|---|---|---|
| 5002.9 | 1368.1 | 10.257 | 0.000 | 12.059 | 5661.0 | 710.0 | 11.183 | 3.613 | 12.907 |
| 5053.2 | 1317.8 | 10.274 | 0.000 | 12.087 | 5711.7 | 659.3 | 11.194 | 3.620 | 12.922 |
| 5103.6 | 1267.4 | 10.285 | 0.000 | 12.113 | 5813.2 | 557.8 | 11.213 | 3.634 | 12.947 |
| 5153.5 | 1217.5 | 10.289 | 0.000 | 12.139 | 5863.9 | 507.1 | 11.222 | 3.640 | 12.959 |
| 5153.5 | 1217.5 | 11.043 | 3.504 | 12.704 | 5914.6 | 456.4 | 11.229 | 3.645 | 12.969 |
| 5204.6 | 1166.4 | 11.059 | 3.519 | 12.729 | 5965.3 | 405.7 | 11.236 | 3.650 | 12.978 |
| 5255.3 | 1115.7 | 11.072 | 3.531 | 12.753 | 6016.0 | 355.0 | 11.242 | 3.654 | 12.986 |
| 5306.0 | 1065.0 | 11.085 | 3.543 | 12.776 | 6066.7 | 304.3 | 11.248 | 3.658 | 12.993 |
| 5356.8 | 1014.2 | 11.098 | 3.555 | 12.798 | 6117.4 | 253.6 | 11.252 | 3.661 | 12.999 |
| 5407.5 | 963.5 | 11.117 | 3.566 | 12.819 | 6168.1 | 202.9 | 11.256 | 3.663 | 13.004 |
| 5458.2 | 912.8 | 11.132 | 3.576 | 12.839 | 6218.9 | 152.1 | 11.259 | 3.665 | 13.007 |
| 5508.9 | 862.1 | 11.146 | 3.586 | 12.857 | 6269.6 | 101.4 | 11.261 | 3.667 | 13.010 |
| 5559.6 | 811.4 | 11.159 | 3.596 | 12.875 | 6320.3 | 50.7 | 11.262 | 3.668 | 13.012 |
| 5610.3 | 760.7 | 11.172 | 3.604 | 12.892 | 6371.0 | 0.0 | 11.262 | 3.668 | 13.012 |
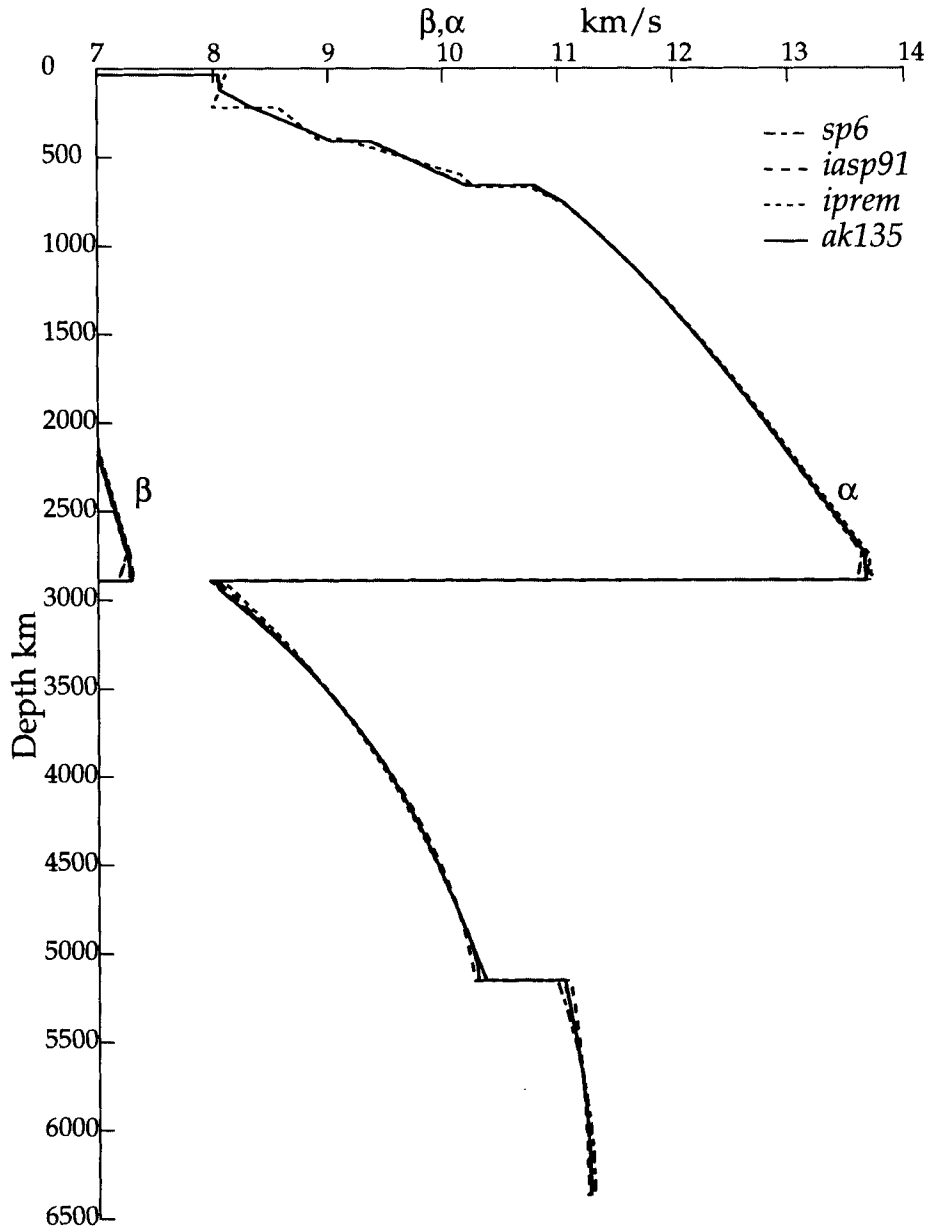


**Figure 12.** Comparison of model *ak135* with other whole earth models.

## REFERENCES

Buland, R. & Chapman, C.H., 1983. The computation of seismic travel times, *Bull. seism. Soc. Am.,* **73,** 1271–1302.

Creager, K.C., 1992. Anisotropy of the inner core from differential times of the phases *PKP* and *PKIKP, Nature,* **356,** 309–314.

Dziewonski, A.M. & Anderson, D.L., 1981. Preliminary Reference Earth Model, *Phys. Earth planet. Inter.,* **25,** 297–356.

Dziewonski, A.M., Hales, A.L. & Lapwood, E.R., 1975. Parametrically simple Earth models consistent with geophysical data, *Phys. Earth planet. Inter.,* **10,** 12–48.

Garnero, E.J., Helmberger, D.V. & Grand, S.P., 1993. Constraining outermost core velocity with *SmKS* waves, *Geophys. Res. Lett.,* **20,** 2463–2466.

Herrin, E., 1968. Introduction to '1968 Seismological Tables for *P*-phases', *Bull. seism. Soc. Am.,* **58,** 1193–1195.

Jeffreys, H. & Bullen, K.E., 1940. *Seismological Tables,* British Association for the Advancement of Science, London.

Kaneshima, S., Hirahara, K., Ohtaki, T. & Yoshida, Y., 1994. Seismic structure near the inner core–outer core boundary, *Geophys. Res. Lett.,* **21,** 157–160.

Kennett, B.L.N., 1991. *IASPEI 1991 Seismological Tables,* Research School of Earth Sciences, Australian National University.

Kennett, B.L.N. & Engdahl, E.R., 1991. Traveltimes for global earthquake location and phase identification, *Geophys. J. Int.,* **105,** 429–465.

McSweeney, T.J., Creager, K.C. & Merrill, R.T., 1995. Inner-core seismic anisotropy and implications for the geodynamo, *Phys. Earth planet. Inter.*

Morelli, A. & Dziewonski, A.M., 1993. Body-wave traveltimes and a spherically symmetric *P*- and *S*-wave velocity model, *Geophys. J. Int.,* **112,** 178–194.

Shearer, P.M. & Toy, K.M., 1991. *PKP(BC)* versus *PKP(DF)* differential travel times and aspherical structure in the Earth's inner core, *J. geophys. Res.,* **96,** 2233–2247.

Song, X. & Helmberger, D.V., 1995. A *P*-wave model of the Earth's core. *J. geophys. Res.* in press.

Widmer, R., 1991. The large scale structure of the deep Earth as constrained by free oscillation observations, *PhD thesis,* University of California, San Diego.